

RESEARCH

Open Access



# Intra-prostatic tumour evolution, steps in metastatic spread and histogenomic associations revealed by integration of multi-region whole-genome sequencing with histopathological features

Srinivasa Rao<sup>1,5\*</sup>, Clare Verrill<sup>1†</sup>, Lucia Cerundolo<sup>1</sup>, Nasullah Khalid Alham<sup>1</sup>, Zeynep Kaya<sup>2</sup>, Miriam O'Hanlon<sup>1</sup>, Alicia Hayes<sup>1</sup>, Adam Lambert<sup>1</sup>, Martha James<sup>1</sup>, Iain D. C. Tullis<sup>3</sup>, Jane Niederer<sup>1</sup>, Shelagh Lovell<sup>1</sup>, Altan Omer<sup>1</sup>, Francisco Lopez<sup>1</sup>, Tom Leslie<sup>1</sup>, Francesca Buffa<sup>3</sup>, Richard J. Bryant<sup>1</sup>, Alastair D. Lamb<sup>1</sup>, Boris Vojnovic<sup>3</sup>, David C. Wedge<sup>4</sup>, Ian G. Mills<sup>1</sup>, Dan J. Woodcock<sup>1</sup>, Ian Tomlinson<sup>3</sup> and Freddie C. Hamdy<sup>1</sup>

## Abstract

**Background** Extension of prostate cancer beyond the primary site by local invasion or nodal metastasis is associated with poor prognosis. Despite significant research on tumour evolution in prostate cancer metastasis, the emergence and evolution of cancer clones at this early stage of expansion and spread are poorly understood. We aimed to delineate the routes of evolution and cancer spread within the prostate and to seminal vesicles and lymph nodes, linking these to histological features that are used in diagnostic risk stratification.

**Methods** We performed whole-genome sequencing on 42 prostate cancer samples from the prostate, seminal vesicles and lymph nodes of five treatment-naïve patients with locally advanced disease. We spatially mapped the clonal composition of cancer across the prostate and the routes of spread of cancer cells within the prostate and to seminal vesicles and lymph nodes in each individual by analysing a total of > 19,000 copy number corrected single nucleotide variants.

**Results** In each patient, we identified sample locations corresponding to the earliest part of the malignancy. In patient 10, we mapped the spread of cancer from the apex of the prostate to the seminal vesicles and identified specific genomic changes associated with the transformation of adenocarcinoma to amphicrine morphology during this spread. Furthermore, we show that the lymph node metastases in this patient arose from specific cancer clones found at the base of the prostate and the seminal vesicles. In patient 15, we observed increased mutational burden, altered mutational signatures and histological changes associated with whole genome duplication. In all patients in whom histological heterogeneity was observed (4/5), we found that the distinct morphologies were located on separate branches of their respective evolutionary trees.

<sup>†</sup>Srinivasa Rao and Clare Verrill contributed equally to this work.

\*Correspondence:

Srinivasa Rao

Srinivasa.rao@nds.ox.ac.uk

Full list of author information is available at the end of the article



© The Author(s) 2024. **Open Access** This article is licensed under a Creative Commons Attribution 4.0 International License, which permits use, sharing, adaptation, distribution and reproduction in any medium or format, as long as you give appropriate credit to the original author(s) and the source, provide a link to the Creative Commons licence, and indicate if changes were made. The images or other third party material in this article are included in the article's Creative Commons licence, unless indicated otherwise in a credit line to the material. If material is not included in the article's Creative Commons licence and your intended use is not permitted by statutory regulation or exceeds the permitted use, you will need to obtain permission directly from the copyright holder. To view a copy of this licence, visit <http://creativecommons.org/licenses/by/4.0/>. The Creative Commons Public Domain Dedication waiver (<http://creativecommons.org/publicdomain/zero/1.0/>) applies to the data made available in this article, unless otherwise stated in a credit line to the data.

**Conclusions** Our results link histological transformation with specific genomic alterations and phylogenetic branching. These findings have implications for diagnosis and risk stratification, in addition to providing a rationale for further studies to characterise the genetic changes causally linked to morphological transformation. Our study demonstrates the value of integrating multi-region sequencing with histopathological data to understand tumour evolution and identify mechanisms of prostate cancer spread.

**Keywords** Prostate cancer, Cancer evolution, Histopathology, Prostate cancer metastasis, Intra-tumour heterogeneity, Spatial genomic analysis

## Background

Prostate cancer is a complex disease with different clinical outcomes depending on the spread of the tumour to local and distant sites. We need better risk stratification of prostate patients to improve prognostic accuracy and enhance therapeutic strategies. Histopathological grading is an important predictor of prostate cancer prognosis. However, current pathological assessment consists of subjective morphological observations made by one or more pathologists. The limitations of the Gleason scoring system are well documented [1–4] and patients with the same Gleason grades can have markedly differing outcomes, especially those with intermediate ISUP Grade Group 2 and 3 disease [5]. Histopathological assessment alone is incompletely predictive and prognostic, and there is an increasing need for multimodal assessment of prostate cancer.

Prostate cancer is characterised by extensive intra-tumoural heterogeneity [6] with evidence of varying molecular expression [7] and mutational profiles [8] in different regions of the tumour. Recent genomic studies have detailed the evolutionary trajectories of metastatic prostate cancer and shown the utility of multi-region sampling to identify molecular features that underlie intra-tumour heterogeneity [8–11]. However, the genomic changes that occur as cancer spreads through the prostate and during local invasion and early metastasis, and their relation to histopathology remain poorly understood.

Although spatial transcriptomics has been used to trace cancer evolution linking specific clones to specific anatomical locations, this technology is currently limited to the identification of copy number alterations (CNAs). As somatic small nucleotide variant (SNV) information is also necessary for comprehensive phylogenetic reconstruction, spatial transcriptomics provides an incomplete picture of cancer evolution. Recent advances in spatial DNA sequencing methods [12, 13] could help address this gap—however, they are currently limited to CNAs and known SNVs. Hence, multi-region whole-genome sequencing is still the method of choice to delineate clonal evolution of cancer. Recently, Nurminen et al. tracked prostate cancer using multi-region

whole-genome sequencing in 2 patients, linking lymph node metastases to specific anatomic sites [14], showing the potential for obtaining clinically relevant insights from a limited number of patients.

Previous studies have shown a relationship between histopathological and genomic features in pan-cancer datasets [15, 16]. Prostate cancer is characterised by histopathological and molecular heterogeneity and a relationship between them would be of clinical interest. In particular, such a relationship has not been examined from a cancer evolution perspective. Hence, we aimed to perform multi-region sequencing to understand the relationship between histopathological transformation and clonal evolution in prostate cancer, linking both to lymph node metastases.

In this study, we analysed five treatment-naive patients with locally advanced prostate cancer and no evidence of distant metastases. We systematically sampled tumour tissue from the prostate, seminal vesicles and local lymph nodes and used whole-genome sequencing to reconstruct the tumour phylogeny in these individuals. By integrating detailed histopathological and spatial information with genomic data, we identified genomic alterations that are associated with location and changes in tissue morphology.

## Methods

### Sample description

Male patients enrolled at the Oxford University Hospitals, aged 50–70 years, with prostate cancer were included in this study. Patients with extra-prostatic cancer spread (beyond the prostate capsule and/or seminal vesicle or lymph node involvement) were selected for sequencing; data from one patient were excluded due to low tumour purity. Data from 5 patients (42 prostate cancer samples, and 1 additional sample determined to be non-cancerous by histopathology) are shown here. No randomisation or blinding were performed as these were not applicable. Fresh frozen prostate samples were acquired from surgically resected (radical prostatectomy) specimens using a previously published method [17]. Lymph node and seminal vesicle metastases were additionally sampled when these structures

were macroscopically involved by tumour, and care was taken that diagnostic processes would not be affected by biobanking. All samples were snap frozen in liquid nitrogen and stored at  $-80^{\circ}\text{C}$  temporarily before being transferred to liquid nitrogen. After biobanking, specimens were processed for routine diagnostics by fixation in neutral buffered formalin for approximately 24 h. Whole blood was collected at the time of surgery for germline DNA and stored at  $-80^{\circ}\text{C}$ . The samples were processed and whole-genome sequencing was performed as described below. They were analysed for single nucleotide variants, copy number alterations and structural variants.

### Sample processing

Serial frozen sections were cut from OCT-embedded tissue and every 4th section was stained for H&E and analysed tumour content by a specialist urological pathologist. Frozen sections were stored again at  $-80^{\circ}\text{C}$  until nucleic acids extraction. DNA and RNA were extracted from the frozen sections using the Quick-DNA/RNA Miniprep Plus Kit (Zymo, D7003) according to the manufacturer's recommendations. Briefly, 1X DNA/RNA Shield + proteinase K was added to the frozen sections and incubated at  $50^{\circ}\text{C}$  for 3 h, followed by lysis and column extraction. Germline DNA was extracted from whole blood, also using the Quick-DNA/RNA Miniprep Plus Kit as above. DNA was quantified using a Qubit HS dsDNA kit (Thermo Scientific) and quality was assessed using a TapeStation (Agilent Technologies).

### Whole-genome sequencing and data pre-processing

DNA libraries were prepared and sequenced as 150-bp paired-end reads by the Oxford Genomics Centre, Wellcome Centre for Human Genetics, Oxford, on the Illumina NovaSeq 6000 using a PCR-free library preparation protocol or all samples except one (details in Additional file 3). PCR amplification was performed for the sample with DNA quantity insufficient for the PCR-free protocol. The median depth of sequencing was 88X for the tumour samples and 33X for the germline samples respectively. DNA libraries were prepared using the NEBNext Ultra II DNA Library Prep Kit for Illumina (New England Biolabs #E7645L) according to the manufacturer's recommendations. Briefly, genomic DNA was fragmented and the ends were repaired enzymatically. Following this, adaptors were ligated, and the resulting library was cleaned up with NEBNext Sample Purification Beads. These libraries were used for sequencing in the PCR-free protocol. For samples requiring amplification, these libraries were PCR-amplified and cleaned up using NEBNext Sample Purification Beads.

### Sample processing and library preparation for FFPE samples

Pathologist-marked regions of interest were manually dissected and pooled from 5X serial sections ( $4\ \mu\text{m}$ ) of formalin-fixed paraffin embedded radical prostatectomy samples. These dissected samples were then used for an extraction-free WGS library preparation method modified from Ellis et al. [18]. Briefly, samples were manually dissected using histology-guided markings and pooled from  $5\times 4\ \mu\text{m}$  FFPE sections. The samples were deparaffinised and lysed in a lysis buffer (Tris-HCl: pH 8.0 30 mM, Tween-20: 0.5%, IGEPAL CA-630: 0.5%) containing Proteinase K (20 mg/ml) and incubated at  $65^{\circ}\text{C}$  on a heating block for 2–3 h. Following lysis, the samples were size selected using Ampure XP Beads and fragmented and end-repaired for 12 min using the NEB Ultra II FS enzyme. The end-repaired DNA samples were ligated with custom adapters described in Ellis et al. and amplified with single-indexed primers to generate WGS libraries for Illumina sequencing. The individual libraries were pooled and sequenced as 150-bp paired-end reads on the Illumina NovaSeq 6000 sequencer at Wales Gene Park, Cardiff. The median depth of sequencing for the FFPE samples was 60X.

### Data pre-processing

Raw data in the form of FASTQ files were adapter-trimmed using BBDuk [19] (v38.79–0) and pre- and post-trim quality was checked using FastQC [20] (v0.11.8). Reads were aligned to the reference genome (hg37) using BWA-MEM [21] (v0.7.17) and coordinate-sorted using Samtools [22] (v1.9). Aligned reads from all samples (PCR-free as well as PCR-amplified) were duplicate marked using Genome Analysis ToolKit (GATK) [23] (v4.1.4.0) MarkDuplicates.

### SNV calling

Base Quality Score Recalibration (BQSR) was performed on duplicate marked bam files and simple somatic mutations (SNVs and short indels) calling was performed with GATK Mutect2 in multi-tumour mode (i.e. by calling somatic mutations in all samples from a patient simultaneously) according to the GATK Best Practices Workflow. Calls from Mutect2 were filtered using GATK FilterMutectCalls. SNVs were further shortlisted for subclone analysis by using a TLOD (log-likelihood of a variant being somatic) threshold of 7.

### CNA calling

Allele-specific subclonal copy number calling was performed using the Battenberg R package [24] (v2.2.9) from the base quality recalibrated, duplicated marked bam

files. Default parameters were used initially to generate copy number profiles. These were used to run subclonal analysis as follows, and the resultant CCF values for each SNV were plotted along the genome as a quality check. Regions of the genome were found to contain errors in CCFs if CCFs were less than surrounding regions in case of incorrect calls of amplification/gain suggesting overcorrection, or CCFs were greater than the surrounding regions in case of incorrect calls of LOH/deletion suggesting undercorrection. In addition, the expected purity of the sample was estimated by adjusting the CCF of the truncal cluster to  $\sim 1$ . Where the original CNA calls were found to be incorrect using these two checks, Battenberg was run again with rho and ploidy presets and checked again for accuracy iteratively. In cases where the tumour purity was too low to call CNAs with Battenberg (lymph nodes 5A\_LN, 6A\_LN, 7A\_LN in patient #02, PPF\_LN in patient #13), the most common CNA profile from the intra-prostatic samples was applied, and a quality check was performed as above to confirm that this is a reasonable assumption to make. Percent subclonality was calculated by dividing the total number of bases with subclonal copy number changes with the total number of bases analysed.

#### Phylogenetic analysis

The DPCLust-3p R package [25] (v1.0.8) was used to pre-process the SNVs (Mutect2) and copy number calls (Battenberg) from each sample and generate loci with CCF (allele fraction corrected by the corresponding copy number for that location). Following this, the CCFs of the loci were clustered using the BayesianGaussian-Mixture function in the Scikit-Learn Python package [26] (v0.24.2) using 1000 iterations. The median value of each cluster was considered to be the corresponding clonal fraction for that subclone. Clusters thus identified were further split or merged by visual inspection where deemed necessary (e.g. when a cluster was visually determined to be composed of multiple sub-clusters). From the CCFs of clones thus obtained, phylogenetic trees were constructed using the sum and crossing rules as described previously [27]. Briefly, the sum rule states that the sum of CCFs of daughter clones should be less than the CCF of the parent clone. If this is not the case, the daughter clone with the smaller number of mutations is a descendant of the other daughter clone. The crossing rule, applicable in multi-region sequencing, states that when clones B and C are daughter clones of clone A, and  $CCF(B) > CCF(C)$  in one sample and  $CCF(C) > CCF(B)$  in another sample, B and C must be cloned on different branches of the phylogenetic tree. Where the sum and crossing rules contradicted each other, a solution that

violated the fewest rules was chosen, to allow for inherently noisy biological data.

#### Construction of clone maps

Clonal composition of each tumour sample was illustrated as a sunburst plot using Plotly [28] (v5.3.1). Corrections were applied to the CCFs based on the solution calculated, as described above, to simplify visualisation. Actual CCFs are presented in the supplementary data (Additional file 2).

#### Mutation signature analysis

Mutational signatures were identified using the DeconstructSigs [29] (v1.8.0) R package. SNVs were grouped into separate bins based on their cluster annotation and each group was processed as a separate 'sample'. COSMIC v3 trinucleotide signatures were used as the reference.

#### Structural variant analysis

Structural variants were called using Svaba [30] (v1.1.0) using default parameters in multi-tumour mode.

#### Fusion validation

TMPRSS2:ERG gene fusion was validated in all samples of patient #08 using the workflow described by Hafstað et al. [31].

#### Software

All analyses were performed in R [32] (v4.2.1) and Python [33] (v3.9.6).

#### Database sources

Prostate cancer-specific driver mutations were downloaded from Intogen [34].

#### Immunohistochemistry staining

##### *PTEN and P-Histone H3 (PHH3) immunohistochemistry (IHC)*

PTEN and PHH3 IHC was performed on a Bond RX autostainer (Leica Biosystems) using a 2-day protocol. On day 1, slides of formalin-fixed paraffin-embedded sections were loaded into the Bond Rx autostainer. The slides were deparaffinised with Leica Dewax solution (AR9222). Epitope Retrieval was performed using Solution 1 (AR9961): 30 min for PTEN IHC and 20 min for P-Histone H3 IHC. Endogenous peroxidase was blocked using Bond Polymer Refine Detection Kit DS9800. The slides were unloaded from the Bond Rx. For PTEN IHC, 100  $\mu$ l of PTEN Rabbit monoclonal antibody (Cell Signaling 138G6) diluted 1/200 in Leica Antibody Diluent (AR9352) was applied to the sections. For PHH3 IHC, antibody (Cell Signaling 9701S) diluted 1/100 in Leica Antibody Diluent (AR9352) was applied. The sections

were incubated overnight at 4 °C in a humidity chamber. On day 2, the slides were loaded into the Bond Rx auto-stainer and the post primary steps were completed using the Bond Polymer Refine Detection Kit (Leica DS9800). For Ki-67 staining, Leica RTU Ki67 PA0410 antibody was used at a dilution of 1:200, epitope retrieval for 20 min, using the JR Bond protocol F+enhancer (includes 15-min antibody incubation). Scoring of PTEN IHC was done by a board certified pathologist (CV) using H-Scoring [35] which involves assessment of intensity (0–3) and proportion score (0–100%).

### PSMA immunohistochemistry

Formalin-fixed paraffin-embedded sections were heated to 60 °C for 10 min, deparaffinised in xylene and rehydrated in graded concentrations of ethanol. Endogenous peroxidase was neutralised with 3% H<sub>2</sub>O<sub>2</sub> in methanol for 10 min at room temperature. Antigen was retrieved using citrate buffer pH 6 for 10 min at 95 °C and samples were left to cool in the buffer for 20 min. Samples were blocked with PBS/5% NGS for 30 min at room temperature. Mouse PSMA monoclonal antibody (Gene Tex GTX19071) diluted 1/100 in PBS/5% NGS was applied to the samples overnight at 4 °C. The sections were then incubated with biotinylated goat anti mouse IgG

(Vectorlabs BA-9200) diluted 1/250 in PBS/5% NGS for 30 min at room temperature. The detection system was ABC reagent (Vectorlabs PK-7100) and DAB Substrate Kit SK-4100 (Vectorlabs). Counterstain was Harris's haematoxylin.

### Image analysis

Stained slides were scanned on the Hamamatsu scanner and analysed using the VisioPharm image analysis platform. Different regions of tumour were annotated by the pathologist (CV). A small subset of immune (H&E) or positive staining cells (IHC) cells were manually selected for training a model which was then used to count the number of immune cells in each annotated region.

## Results

### Multi-region sampling strategy and data integration

We performed whole-genome sequencing on fresh-frozen tissue samples of the prostate, seminal vesicles and lymph nodes (Table 1, Fig. 1A) to a median tumour depth of 88X using the Illumina platform (see methods for details). We systematically collected multiple samples as punches from the prostate in all cases based on histopathological evidence of tumour and from the seminal vesicles and lymph nodes where possible. We

**Table 1** Summary of clinical characteristics and genomic findings

Patient ID	Serum PSA (ng/L)	Gleason grade group	pTN stage	Fresh frozen samples sequenced#	Length of follow-up	Current clinical status <sup>a</sup>	Main genomic findings
#02	36.8	5	3bN1	P 8 SV 1 + FFPE samples: LN 3	3 years	PPP. Nodal and bone metastases. On ADT + chemotherapy (Docetaxel)	Branching evolution in the prostate. Evolution driven primarily by SNVs; polyclonal SV sample
#08	6.50	5	3bN1	P 6 SV 2	3 years	PPP. Residual pelvic lymph node disease. On ADT + chemotherapy (Docetaxel)	Branching evolution in the prostate. Evolution driven by a number of CNAs in addition to SNVs; FOXP1 deletion in clone spreading to SV; polyclonal SV
#10	5.08	3 (with amphicrine differentiation)	3bN1	P 5 LN 4 SV 0 + FFPE samples: P 3 SV 1	3 years	PPP. Widespread lymph node metastases on CT. On ADT + chemotherapy (Cisplatin/Etoposide)	Branching evolution in the prostate. Amphicrine prostate cancer evolved from Adenocarcinoma;
#13	46.30	3	3bN1	P 5 LN 1	3 years	Recurrent pelvic lymph node and bone metastases. On ADT + chemotherapy (Docetaxel)	Branching evolution in the prostate. No notable histological heterogeneity
#15	6.83	5	3aN1	P 2 LN 2	3 years	Salvage pelvic radiotherapy for rising PSA to 0.29. PSMA-PET negative	Branching evolution in the prostate. Whole genome doubling; chromoplexy; increased SBS3

UICC 8th ed

P prostate, LN lymph node, SV seminal vesicle, ADT androgen deprivation therapy, PPP persistent post-operative prostate-specific antigen (PSA), CT computerised tomography, PSMA prostate-specific membrane antigen

<sup>a</sup> As of February 2023

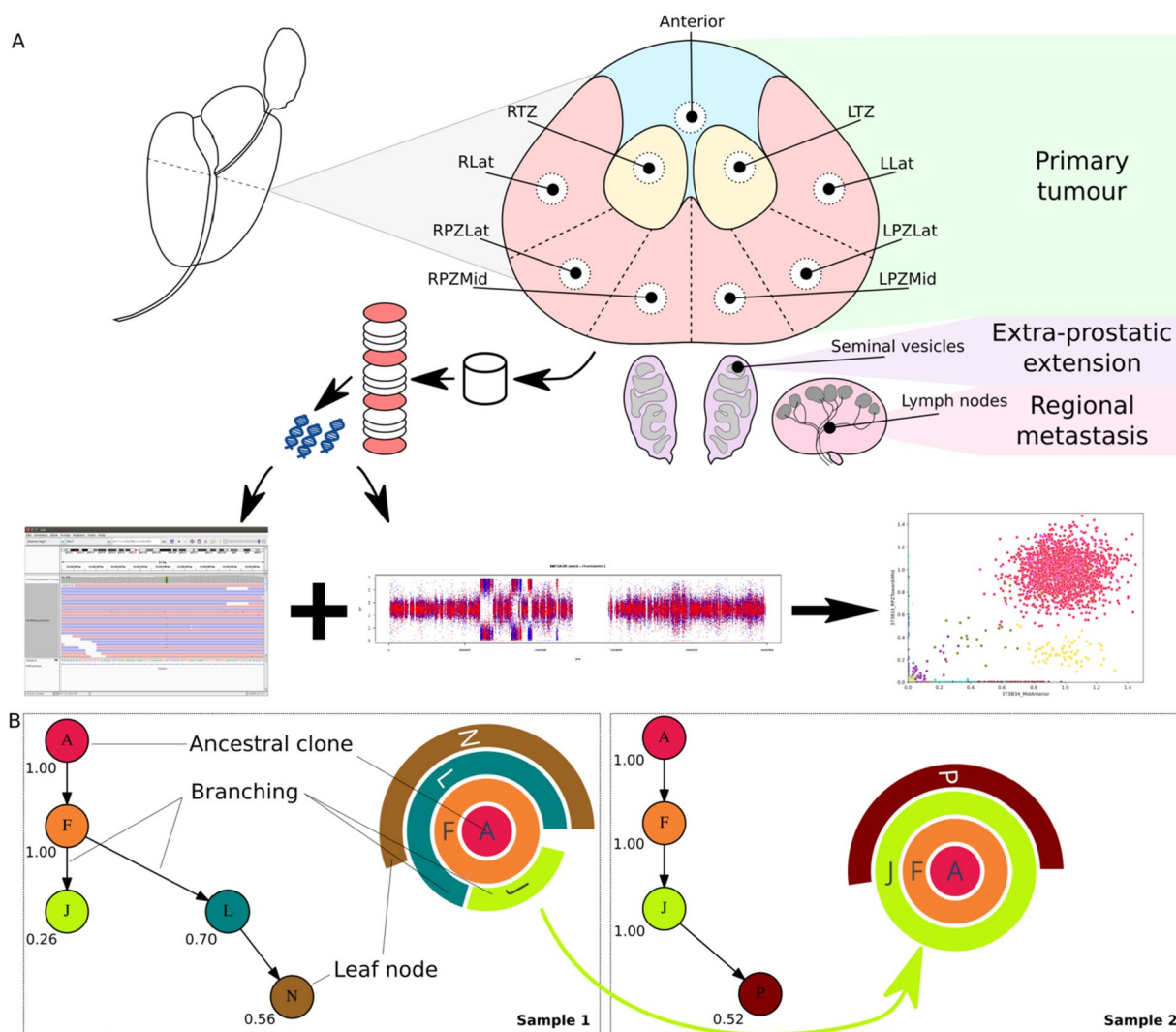


**Fig. 1** **A** Schematic of sample biobanking and processing: A transverse section of the prostate was systematically sampled as 5-mm diameter x 5-mm-thick punches to obtain samples from different regions of the prostate. In addition, samples were collected from the seminal vesicles and local lymph nodes. Punches histologically confirmed to contain tumour cells by H&E staining of intermittent sections, selected histologically normal regions, seminal vesicle and lymph node samples were sequenced over the whole genome. SNVs and CNAs calculated from the WGS data were used to infer the phylogenetic structure of the tumours. **B** Depiction of phylogenetic trees as sunburst plots and determination of evolutionary routes: subclones identified in a sample are depicted as concentric circles/arcs, with the ancestral clone at the centre and each subsequent outer level representing a daughter clone. Multiple subclones at a given level indicate branches on the phylogenetic tree and hence that they are subclonal (cancer cell fraction < 1). Given two adjacent samples, e.g. sample 1 and sample 2, the tumour in sample 1 is inferred to give rise to sample 2 as the cancer cell fraction of clone J increased from 0.26 in the former to 1.00 in the latter

estimated cancer cell purities at 10–90% using the Battenberg algorithm (see methods). We also systematically sampled histologically normal prostate tissue punches in some patients to check for the presence of pre-malignant genomic changes. In some cases, in order to present a more complete picture of tumour spread, we augmented the data from fresh frozen samples by whole-genome sequencing of histopathologically guided sampling of formalin fixed paraffin-embedded tissue from the diagnostic archive.

Using these spatially distinct samples, we built phylogenetic trees based on somatic small nucleotide variants (SNVs) and copy number alterations (CNAs) to assess cancer evolution in each patient. In addition to the overall phylogenetic tree for each patient, we inferred inter-sample clonal relationships based on the median cancer cell fraction of the SNVs in each clone and the spatial context of each sample. We depict the clonal composition of each sample as a sunburst plot (Fig. 1B) and the inter-sample relationships were superimposed on the histology

images of the whole prostate to construct a ‘clone map’ for each patient. We present these results below.

A summary of the somatic mutations in the sequenced samples revealed that *PTEN* is deleted in nearly all samples across the 5 patients (Fig. 2). Further, tumour suppressor (*TP53*, *RB1*) and DNA repair

(*BRCA2*) genes were altered in more than one individual. SNVs and CNAs were commonly present across several samples in each individual, pointing to a shared evolutionary history. Samples from #15 had the highest number of mutations affecting coding regions. We also found a higher proportion of C > T mutations in one of the four samples from #15.

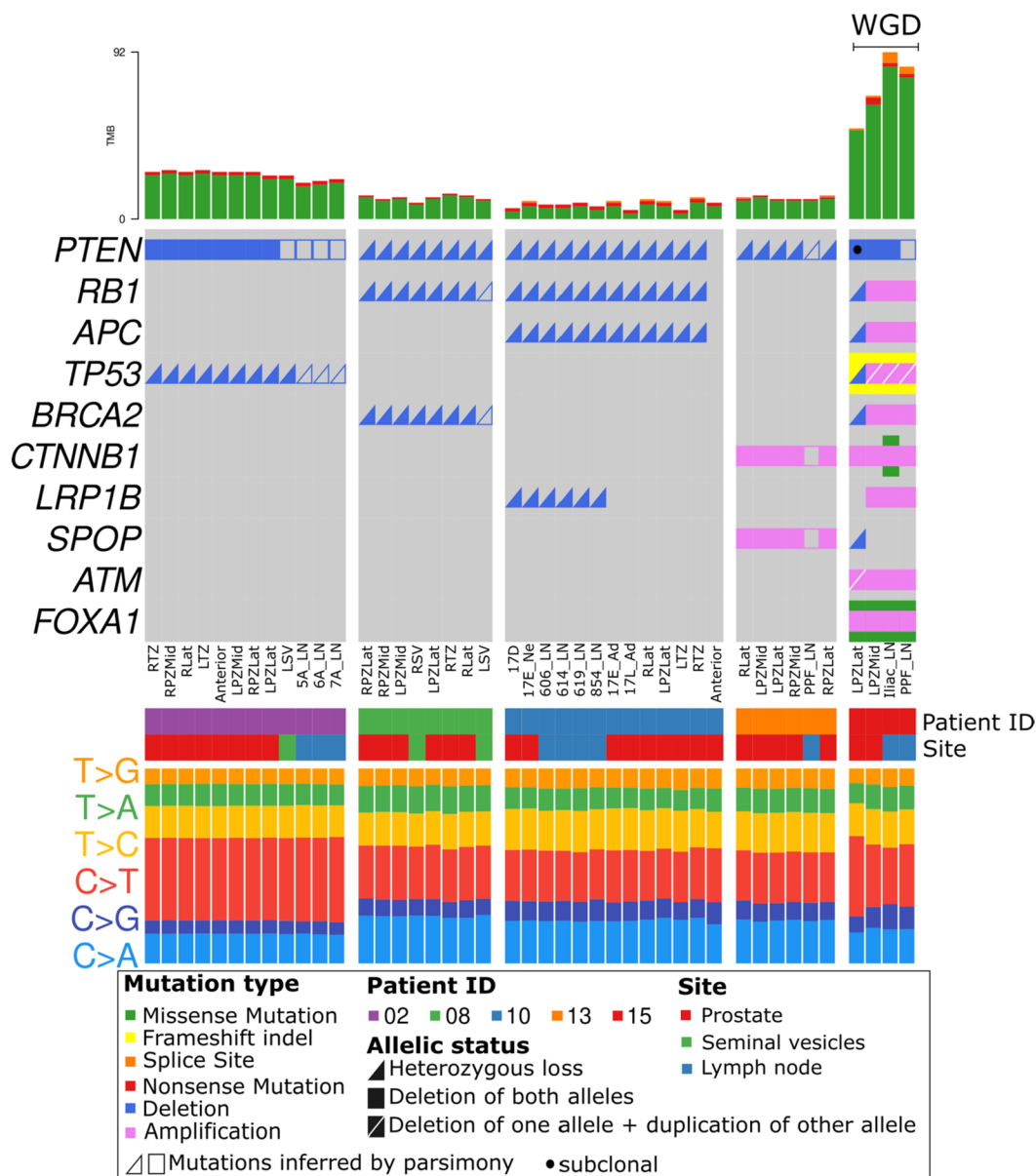


**Fig. 2** Oncoplot summary of SNVs and CNAs affecting known prostate cancer diver genes (Intogen) in the sequenced samples. Samples are grouped by patient ID and annotated for sample site. Integer copy numbers < 2 and > 2 were classified as deletion (Del) and amplification (Amp), respectively. Proportions of the six possible types of mutational conversions in the SNVs are shown at the bottom. Copy number alterations that were not called by Battenberg, but inferred by parsimony and supporting evidence from raw data are shown as unfilled shapes. Mutation type legend applies both to the oncoplot (middle panel) and the TMB plot (top panel) (TMB, total mutation burden; in this figure, refer to SNVs in coding regions)

### Clone maps reveal evolution and spread of cancer cells within the prostate

In patient #02 (Fig. 3A, Additional file 1: Fig. S3, Additional file 1: Fig. S4, Additional file 1: Fig. S20), the LPZLat sample represents the earliest part of the malignancy, with origin of new clones as the cancer spreads along the peripheral zone to the right side. We found that the ancestral clone (clone A) comprising several copy number changes (e.g. 10q23 LOH, 16q22 LOH, 17p13 LOH) eventually gave rise to a number of subclones that were exclusively distinguished by SNVs with no further changes observed in copy number. The cancer in the seminal vesicle sample (LSV) was determined to be polyclonal (defined as a sample consisting of two or more subclones sharing a parent clone), suggesting that this is a result of either multi-clonal invasive spread or seeding from multiple metastatic events. Lymph node metastases arose from Clone A (5A\_LN) and Clone J (6A\_LN, 7A\_LN). Clone J was also the source of the majority of the clonal heterogeneity in this patient, as it gave rise to multiple independent daughter clones (E, I, O, P). However, no copy number changes or SNVs affecting coding genes could be attributed to this clone.

In patient #08 (Fig. 3B, Additional file 1: Fig. S5, Additional file 1: Fig. S6), the earliest tumour location was inferred to be RPZLat and it spread along the peripheral zone to the left. The ancestral clone harboured copy number alterations involving several known driver genes (9p LOH, 10 LOH, 12p13 LOH, 13q14 LOH, 21q22 LOH). A heterozygous partial loss of the ERG gene (chr21:39868781–42856048, corresponding to exons 1–3) and the intervening region between ERG and TMPRSS2 was observed as a truncal event. TMPRSS2:ERG gene fusion was validated in all samples from this patient through analysis of the discordant and soft-clipped reads in this chromosomal region, and the breakpoints were identified as chr21:42856366 (TMPRSS2) and chr21:39867006 (ERG). Several subclonal copy number alterations were also prominent in the leaf nodes (tips) of the evolutionary tree, e.g. 12q24 LOH in clone C, and 6q LOH in clone G, affecting known prostate cancer driver genes (Intogen) such as *NCOR2*, *FOXO3* and *ARID1B*. Clone D in particular harboured a loss of *FOXP1* (3p13 LOH), a known tumour suppressor gene in prostate cancer

[36], and notably, this clone was present in a seminal vesicle sample (LSV). Knockdown of *FOXP1* in LNCaP prostate cancer cells resulted in increased migration in vitro (Additional file 1: Fig. S13). Clone H is the source of the majority of clonal heterogeneity in this patient and is the source of 6 subclones. However, no protein-coding mutations could be attributed to this clone. As in patient #02, the tumour in the seminal vesicles is polyclonal, again suggesting an invasive spread from the prostate.

In patient #13 (Fig. 3C, Additional file 1: Fig. S7, Additional file 1: Fig. S8), RLat represents the earliest region of the tumour, with the tumour spreading along the peripheral zone towards the left. Clone B is the last dominant clone (present in all intra-prostatic samples) and was the source of 3 subclones (C, D, F). Lymph node metastasis (PPF\_LN) was determined to arise from clone C, although low tumour purity in the lymph node sample precluded a more detailed analysis.

### Amphicrine prostate cancer arises from adenocarcinoma

In patient #10, histology of the lymph nodes revealed cancer in 12/22 nodes on the right side and 1/13 nodes on the left side. All nodal disease was amphicrine morphology (Fig. 4A). Of these, four lymph nodes were biobanked and sequenced. Amphicrine cancer is a recently described variant of prostate cancer on the spectrum of neuroendocrine differentiation, where primary cancers display features of both exocrine (classic acinar adenocarcinoma) and neuroendocrine prostate cancer [37, 38]. On standard diagnostic staining, the primary prostate cancer in this case was negative for neuroendocrine markers, but the nodal disease was positive for AR, NKX3.1 (Additional file 1: Fig. S18) and markers of NE differentiation (Synaptophysin, and CD56) (Fig. 4A) with a Ki67 index of 60%. Most of the intra-prostatic malignant tumour was present towards the base of the prostate close to the seminal vesicles. Diagnostic H&E sections from this area revealed the presence of adenocarcinoma and amphicrine carcinoma in the prostate close to and in the base of the seminal vesicles with coexistence of the two histological subtypes (Fig. 4C). The nodal metastatic tumour in this case and some of the primary tumour showed extensive neuroendocrine (NE) differentiation. There was solid/nested growth with some gland formation

(See figure on next page.)

**Fig. 3** **A** Phylogenetic trees and clone maps of patient #02, **B** patient #08, and **C** patient #13, showing diverse routes of tumour evolution within the prostate, local invasion to seminal vesicles, and metastasis to lymph nodes. The phylogenetic trees are annotated with SNVs and CNAs involving known prostate cancer driver genes (Intogen). The numbers on the edges of the phylogenetic tree and the X-axis scale represent the number of SNVs assigned to the daughter clone. Metastatic events to lymph nodes are annotated on the phylogenetic tree with dashed arrows. Clone names are sorted based on cluster size, i.e. A > B > C and so on

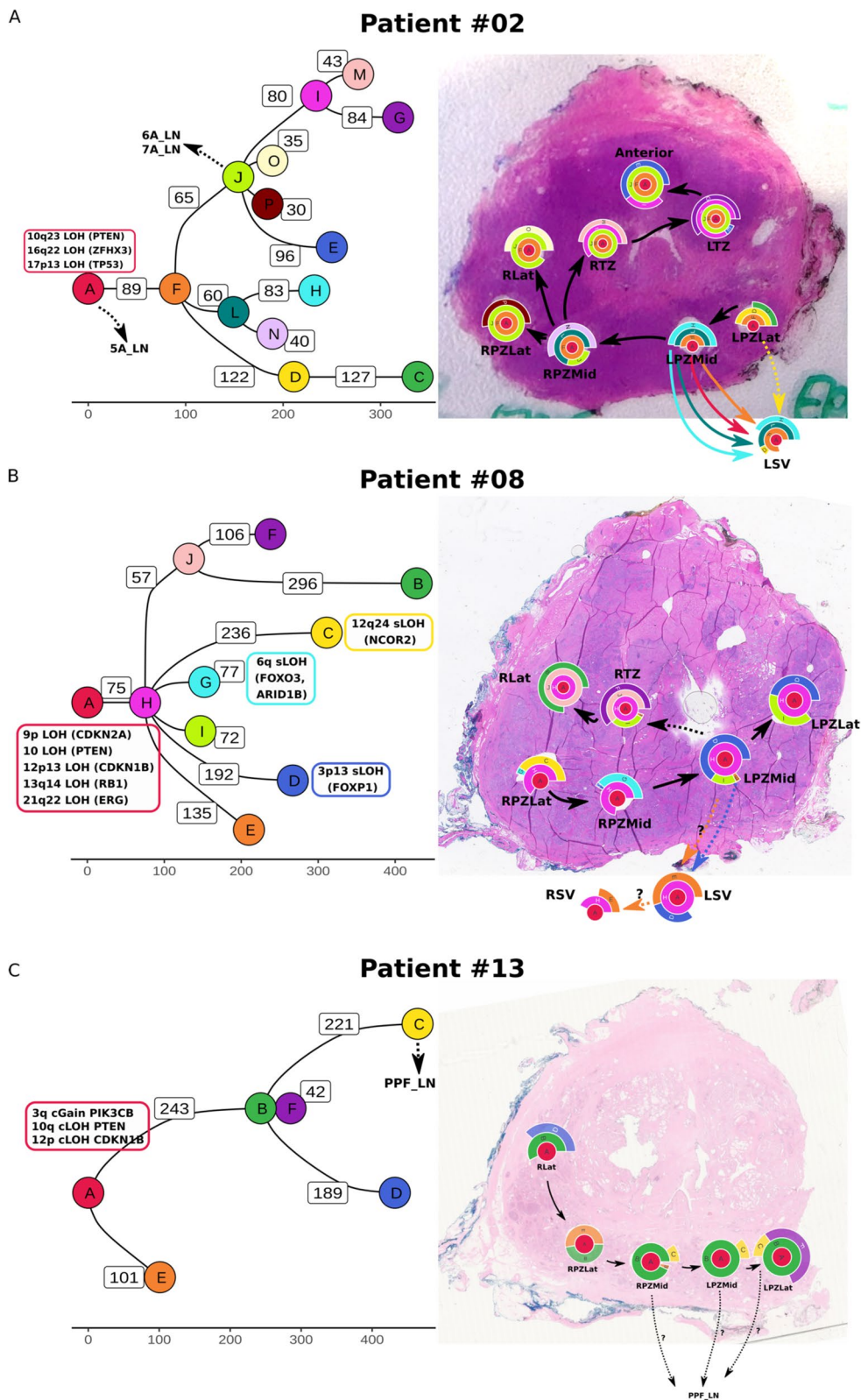


**Fig. 3** (See legend on previous page.)

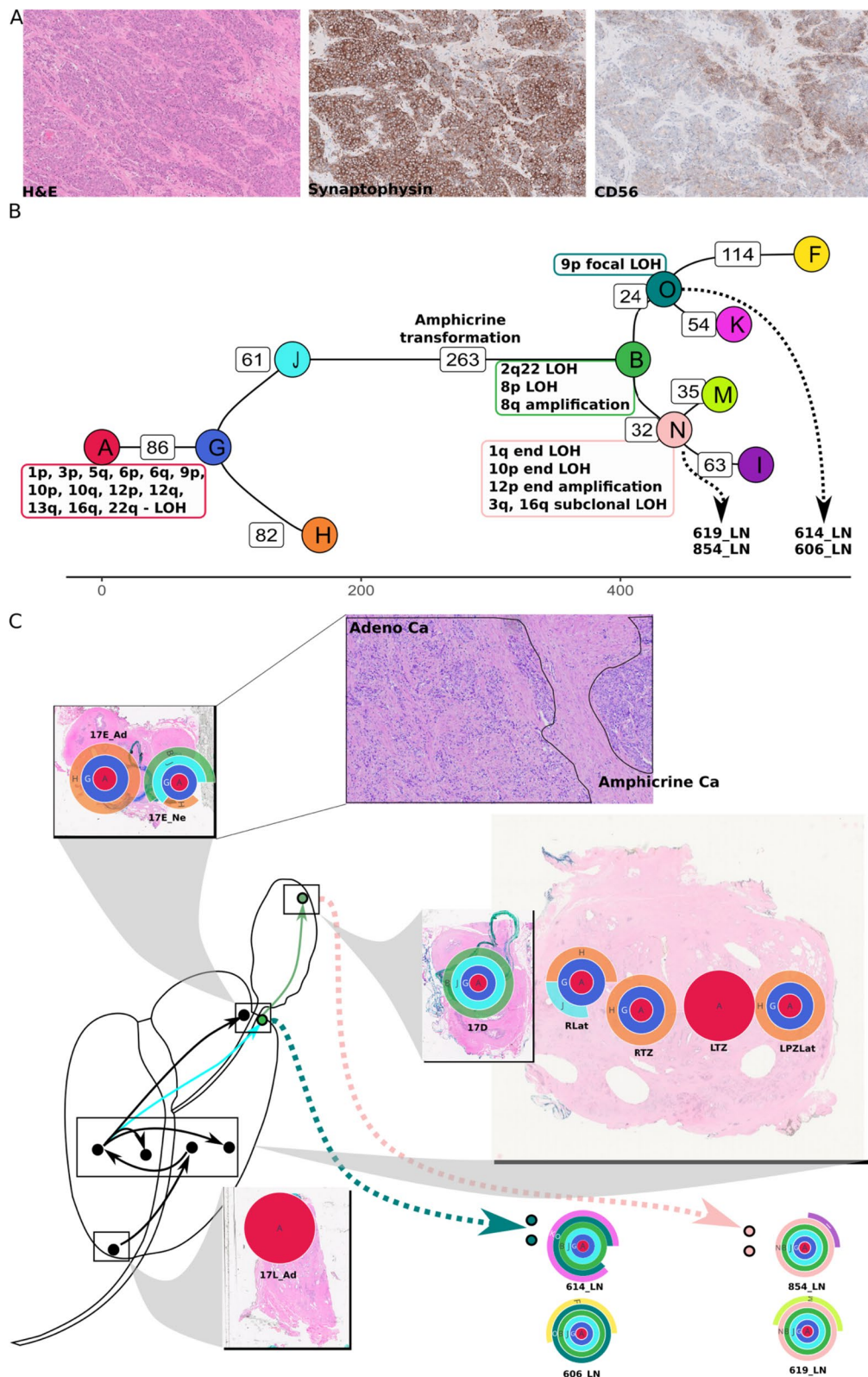


**Fig. 4** **A** Amphilrine morphology in lymph nodes, as seen by H&E staining, immunohistochemistry for Synaptophysin and CD56. **B** Phylogenetic tree for patient #10, with several copy number changes at the branching points. Clones that were likely sources of metastatic seeding are connected to the lymph node sample IDs by dashed arrows. **C** Clone map showing inferred route of cancer progression; clone J in the RLat punch expands in 17E\_Ne and is associated with transformation from adenocarcinoma to amphilrine appearance

in the primary tumour (Fig S19). Cells showed amphiphilic cytoplasm, vesicular nuclei and macronucleoli, without the features of small cell or large cell NE carcinoma. The majority of the nodal metastatic disease showed solid sheets of high grade carcinoma cells with rosettes and small areas of necrosis. The morphological features were not typical of small cell NE carcinoma and were considered those of the relatively recently described entity of ‘Prostate Carcinoma with Amphicrine Features’.

After histology-guided dissection of FFPE sections from the amphicrine and adenocarcinoma regions separately, extracted DNA was sequenced to enable a detailed reconstruction of tumour evolution in this patient. This analysis revealed that the adenocarcinoma transdifferentiated into amphicrine morphology during its spread through the prostate, with prominent genomic changes including the loss of 8p, amplification of 8q and loss of 2q22 (Additional file 1: section 5, Additional file 1: Fig. S9, Additional file 1: Fig. S10). Two seeding events were inferred, leading to metastatic growth in 614\_LN/606\_LN and 619\_LN/854\_LN lymph nodes respectively, based on SNV clustering as well as copy number analysis (Fig. 4B and C). The first seeding event to 614\_LN/606\_LN was inferred from the presence of a focal LOH in 9p23 (affecting the PTPRD gene); this focal LOH was not detected in the other lymph node or intra-prostatic samples. Hence, this CNA was determined to occur prior to or coincident with the emergence of clone O. Due to the features shared with 17E\_Ne, and the absence of features from 17D, the seeding to 614\_LN/606\_LN was inferred to be between these two prostate/seminal vesicle samples. The second seeding event to 619\_LN/854\_LN lymph nodes was inferred by the presence of a shared CNA with 17D (12p end amplification), placing its origin chronologically after 17D. Several copy number changes (1q end LOH, 10p end LOH, 3q and 16q subclonal LOH) are also shared by 619\_LN/854\_LN lymph nodes, suggesting that they were coincident with the emergence of clone N. The clone map for this patient uncovered a complex 3-dimensional evolutionary history, with lymph node metastases arising from or near the seminal vesicles. Copy number analysis revealed telomeric allele imbalance in chromosomes 1q (LOH), 6p (LOH), 8p (LOH) and 12p (gain). In addition, a sample (Anterior punch) annotated as benign by histopathological assessment, but close to the main tumour was found to harbour a mutant clone with ~250 SNVs of a lineage distinct from the main tumour. No prostate cancer-specific driver mutations could be identified to explain the emergence of this clone and no copy number changes were detected.

### Distinct histopathological features and multiple metastatic seeding events to lymph nodes in patient #15

In patient #15, from whom two intra-prostatic and two lymph node samples were analysed, we were able to reconstruct the phylogenetic tree from a complex set of chromosomal gains and losses. PTEN deletion was observed in two samples (LPZMid, Iliac\_LN; chr10:89074486–90215438), subclonal PTEN loss and deletion in one sample (LPZLat; chr10:89001549–90145211, 0+0 in 0.75 fraction subclone and 1+0 0.25 fraction subclone), and PTEN deletion was inferred in PPF\_LN. TP53 frameshift insertion was observed in all samples from this patient. From the clonal composition and the phylogenetic tree (Fig. 5A, B, Additional file 1: Fig. S11, Additional file 1: Fig. S12), we inferred that clone H originated in LPZLat and expanded to become clonal in LPZMid sample. This clone eventually seeded metastasis to both the lymph nodes (Iliac\_LN and PPF\_LN) through its daughter clone A. In addition, two additional seeding events to the PPF\_LN could be inferred, one event from LPZMid (clone I) and another from LPZLat (clone G). The relative timing of these seeding events could not be determined from the data.

In histopathological analysis, the two intra-prostatic regions corresponding to the sequenced samples had a distinctly different morphology, with a clear demarcation between the two (Fig. 5C). The LPZMid sample had a higher Gleason score of 10 (5+5)/grade group 5, versus LPZLat which had a Gleason score of 7 (4+3)/grade group 3. There was also extensive solid pattern intraductal carcinoma adjacent to the LPZMid punch, but not LPZLat. This difference between these two samples was also reflected in the PSMA staining pattern, with minimal or absent staining in the Gleason score 10 areas around LPZTowardsMid (Fig. 5D) (H Score 10) but retained in the Gleason score 7 areas around LPZLat (H Score 100). The cancer metastases in the lymph nodes matched the morphology in LPZMid. There was also a high distribution of tumour infiltrating lymphocytes in the LPZLat sample, whereas TILs were notably less abundant in LPZMid (Fig. 5E).

### Whole genome duplication and extensive chromoplexy distinguish the intra-prostatic samples in #15

Whole genome duplication (WGD) is the doubling of one or both alleles of chromosomes in a usually diploid cell, resulting in triploidy or tetraploidy respectively. We considered the genomes of samples to be doubled (WGD-positive) if their ploidy was greater than 3. Hence, LPZMid, Iliac\_LN and PPF\_LN were found to be WGD-positive. The majority of the chromosomes have 3 or more copies, as seen in the copy number profiles (Fig. 6A). In the sample without whole genome doubling

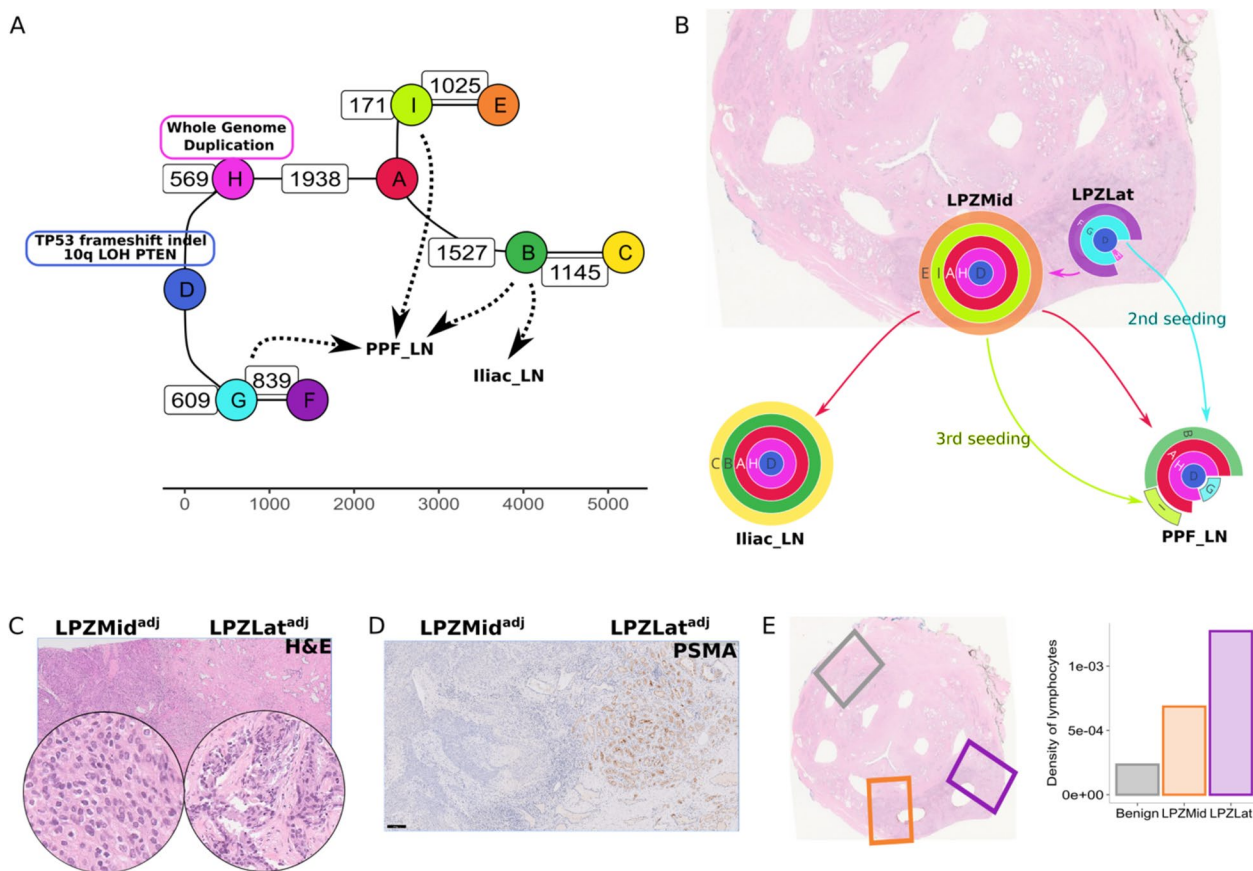


**Fig. 5** **A** Phylogenetic tree for #15 showing clones I, G and C as potential sources of metastatic seeding to lymph nodes. **B** Clone map of patient #15 showing routes of intra-prostatic spread and metastasis to lymph nodes. Clone H (pink) expands to become clonal in LPZMid. **C** A H&E section adjacent to the sequenced samples with areas corresponding to LPZMid and LPZLat on a plane close to the punches (superscripted with *adj* to denote this) showing different morphologies with **D** matching PSMA expression and **E** numbers of tumour-infiltrating lymphocyte counted by image analysis in corresponding regions compared to a distant non-tumour region

(LPZLat, ploidy=2.80), 84% of the genome was subclonal (as opposed to 18% subclonality in LPZMid), suggesting that this sample is composed of a mixture of clones with differing copy number profiles, possibly due to a mix of WGD and non-WGD cancer cell populations. *PTEN* was subclonally hemizygous in this sample as seen by positive IHC staining (Fig. 6B) and copy number profiling (Fig. 6C), in contrast to LPZMid where *PTEN* was completely deleted. Analysis of structural variants revealed several inter-chromosomal translocation events (Fig. 6D) indicating chromoplexy and extensive chromosomal fragmentation suggestive of genomic instability in LPZLat. While several structural variants are shared between LPZLat and LPZMid (corroborating the evolutionary origin of the latter from the former), the number of inter-chromosomal translocations is higher in the former (60 vs 48). Translocations present in the PPF\_LN and LPZLat samples (chr5-chr19, chr13-chr15, chr2-chr5) but not in the LPZMid or Iliac\_LN samples corroborate

the additional metastatic seeding event (clone G) from LPZLat to PPF\_LN as inferred from SNV clustering (Fig. 5A).

**Phylogenetic tree branches in #15 show differences in mutational signatures**

Unlike other individuals, the truncal or ancestral clone in #15 was not the clone with the highest number of mutations (Additional file 1: section 6). Hence, we hypothesised that a new mutational process could have led to an increased mutation rate later in the phylogenetic tree. To investigate this further, we subdivided the SNVs into five groups based on the four sub-sections of the phylogenetic tree (GE, HA, BC, IE) and one truncal clone (D) and analysed their trinucleotide mutational signatures (Fig. 7A). While C>T mutations were the most abundant type in D and GE, this was not the case in HA, BC and IE. Deconvoluting these mutational signatures into known signatures from COSMIC v3.2,

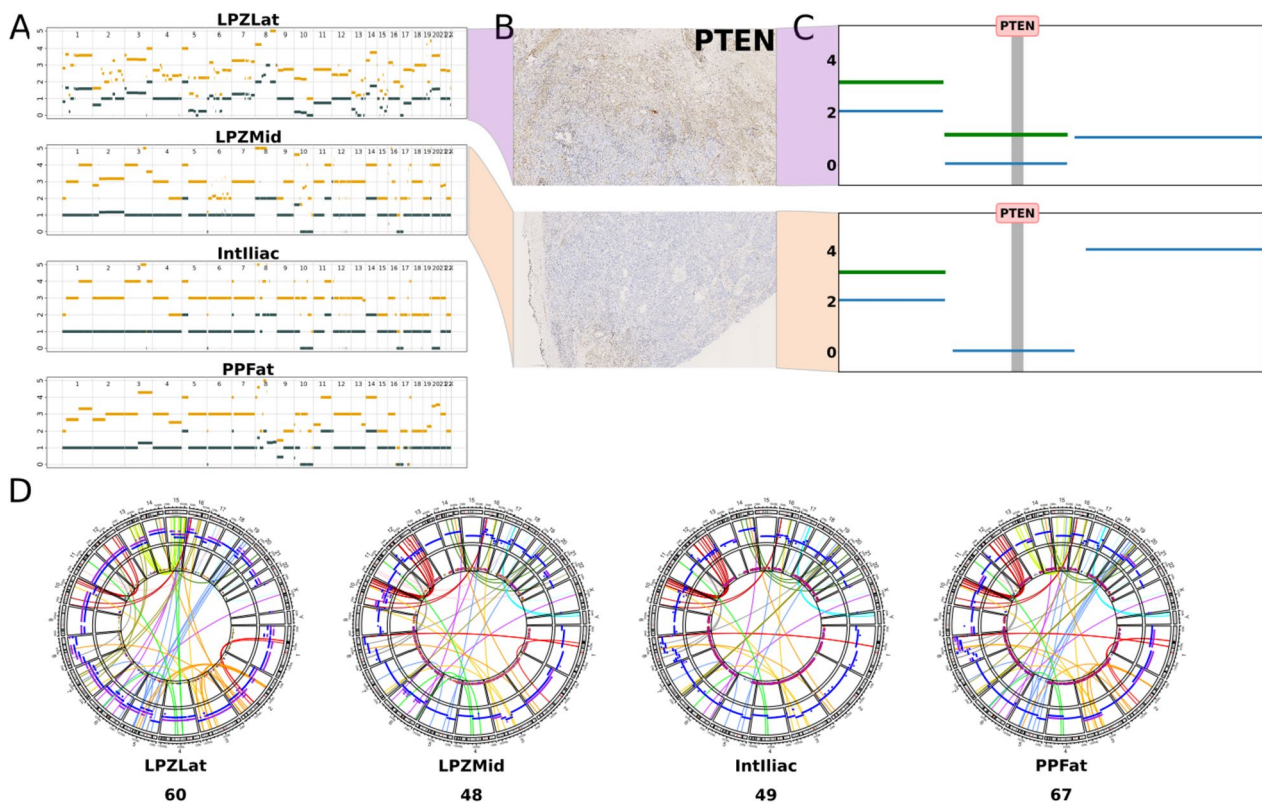


**Fig. 6** **A** Copy number plots for #15 generated by Battenberg showing a subclonal profile for LPZLat and whole genome duplication in LPZMid, Intlliac and PPFat samples. **B** PTEN immunohistochemistry staining corresponding to LPZLat (top) and LPZLatMid (bottom) samples and **C** their corresponding PTEN copy number profiles. **D** Structural variants plotted as circos plots, with different coloured links based on the chromosomes in which the variants' start coordinates are located

we discovered that SBS3 (associated with defective homology directed repair) increasingly contributed to the overall signature in HA, BC and IE (Fig. 7B). This suggests that there is a change in mutational processes starting at clone H. However, *BRCA1* and *BRCA2* genes were intact (Additional file 1: section 8: CNA profiles zoomed in on *BRCA1*, *BRCA2*, *PALB2* loci, Additional file 1: Fig. S14) in LPZMid and there was no evidence of increased methylation in *BRCA1* and *BRCA2* promoter regions (Additional file 1: section 9: Methylation EPIC array data, Additional file 1: Fig. S15). This led us to explore alternative explanations for the increased contribution of SBS3 signature in HA, BC and IE subsections. We observed that the increased contribution of signature SBS3 coincided with whole genome duplication. We also observed increased *PHH3* staining in LPZMid compared to LPZLat (Fig. 7C) indicating a higher number of cells in G2/M in the former region.

#### Histological differences are associated with genomic changes

In order to understand the relationship between genomic changes and histology, we analysed the histological characteristics of the punches and correlated these with their corresponding clonal composition. We observed histological differences in adjacent punches in four patients (Fig. 8). In #02, prominent intraductal carcinoma (IDC) was present in RPZMid in contrast to no IDC in RTZ. Similarly, in #08 predominantly cribriform intraductal carcinoma, Gleason grade 4+4 was present in RPZLat whereas RLat was comprised of a higher Gleason grade tumour (4+5) without cribriform morphology. In #10, adjacent regions within the same FFPE section displayed features of adenocarcinoma and amphicrine carcinoma. In #15, LPZLat consisted of a Gleason grade 4+3 tumour and the neighbouring punch LPZMid was classified as grade 5+5 with no discernible glands. In all these cases, each histological subtype was found to predominantly consist of clones from a separate branch of

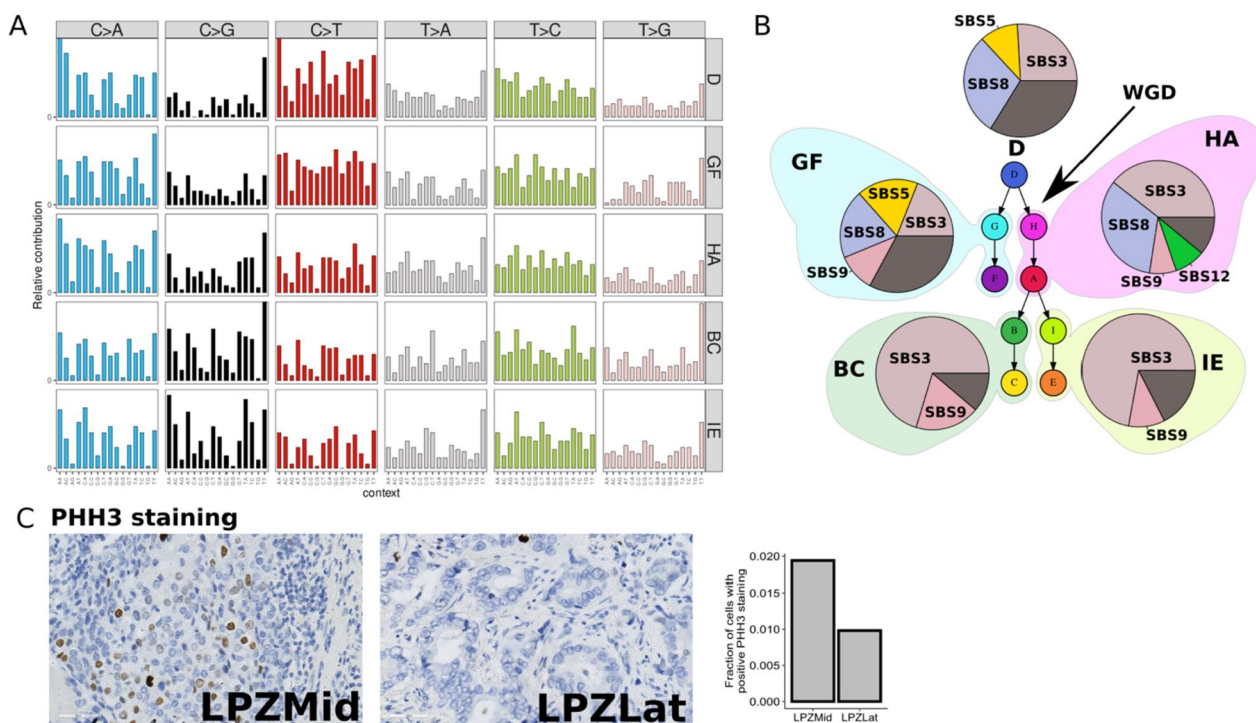


**Fig. 7** **A** Trinucleotide mutational signatures in each subsection of the phylogenetic tree for patient #15. **B** Pie charts showing increasing contribution of signature 3 in tree sub-sections HA, BC and IE compared to D and GF. **C** Immunohistochemical staining for PHH3 (positive in G2/M phase of cell cycle), plotted as the fraction of positive cells, shows a higher proportion in the tissue region corresponding to LPZMid

the phylogenetic tree. We quantified the total number of SNVs uniquely present in either sample in the pair as a measure of the evolutionary distance between the two morphologies—223, 666, 324 and 4582 unique SNVs were seen in patients #02, #08, #10 and #15, respectively.

**Other general findings**

We observed a high degree of branching evolution within the prostate. In patient #02, branching occurs at nodes F, I, J and L resulting in 8 daughter clones within the prostate. In patient #08, branching at nodes H and J results in 7 daughter clones within the prostate. Intra-prostatic branching evolution was also seen to a lesser extent in #10 (at node G), #13 (at nodes A and B) and #15 (at nodes D and A).

We also observed multiple seeding events to lymph node metastases (patient #02, patient #10, patient #15). This raises the possibility that nodal metastatic potential was acquired in a clone that is not most directly associated with a seeding event. For example, in patient #02, while metastatic seeding occurs from clone A (5A\_LN) and clone J (6A\_LN, 7A\_LN), no SNVs were observed in the coding regions of known driver genes and no new copy number alterations were acquired between clone A and J.

In the samples analysed, extensive tumour evolution occurred in the prostate, whereas fewer subclonal clusters could be identified in lymph node samples. However, in patient #10, continued evolution occurred in the lymph nodes with each of the 4 lymph nodes harbouring its own unique subclone.

In all patients except patient #10, the earliest tumour location is in the peripheral zone and the malignancy spreads circumferentially. The patterns of inferred cancer spread within the prostate suggest a predilection for the cancer cells to be limited to the prostate capsule (although there is histological evidence of extraprostatic extension, which is classified as T3a, in limited areas in all the patients in this study). In patient #10, the earliest tumour location is in the apex of the prostate, with lymph node metastases arising from the seminal vesicles.

For the majority of intra-prostatic clones in patient #02, no specific driver mutations (copy number or SNV) could be attributed. Specific driver genes can be attributed to SV invasion in #08 and lymph node metastases in #10.

**Discussion**

Using a systematic approach to biobanking and sequencing analysis, we integrated genomic data with histopathological and spatial information in order to delineate the routes of tumour evolution in intra-prostatic spread,

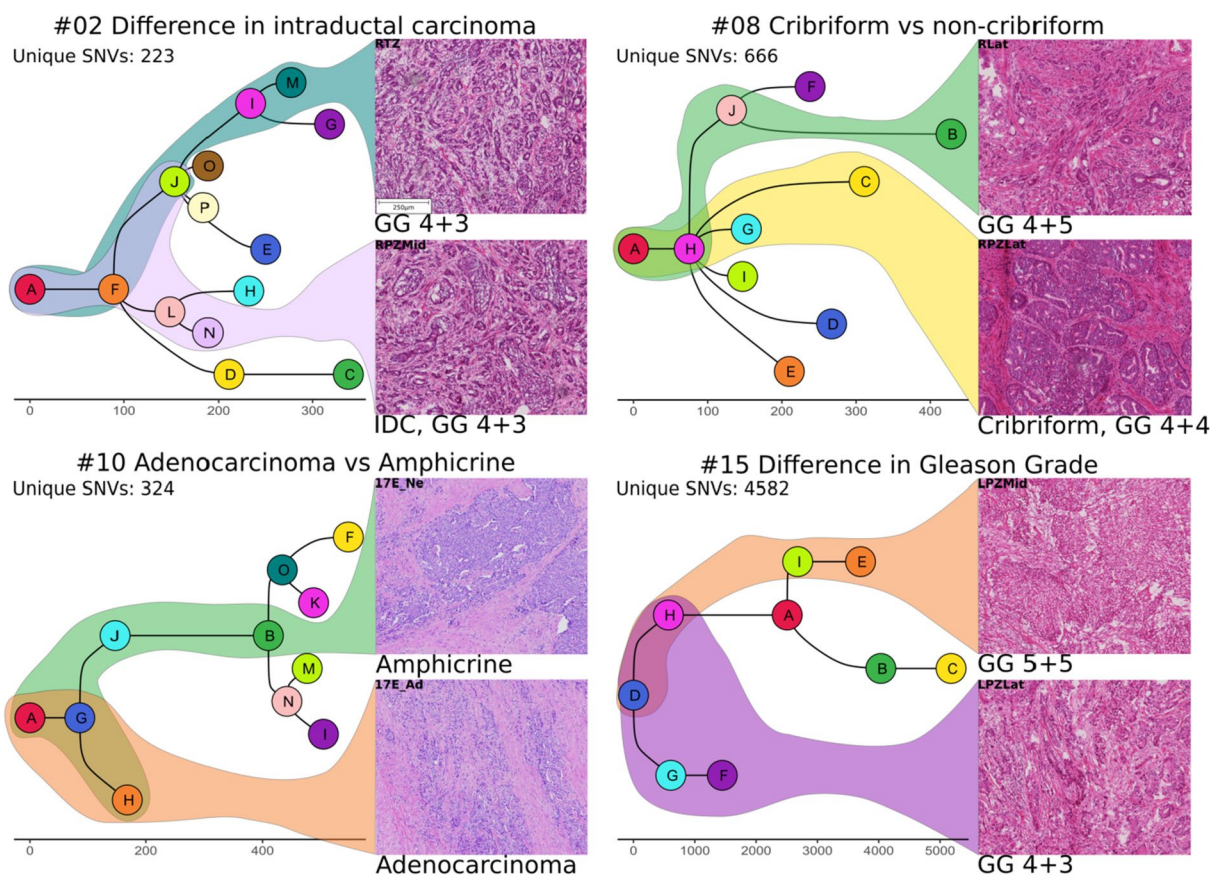


**Fig. 8** Pairs of H&E-stained sections (frozen: #02, #08, #15; FFPE: #10) corresponding to sequenced regions from each of four patients (4x magnification). Histological differences within each pair are highlighted, and the corresponding branches of the phylogenetic trees are shown in the colours of the respective leaf/tip nodes. The total number of SNVs unique to either of the two histologically distinct samples are represented as 'Unique SNVs'. GG, Gleason grade; IDC, intraductal carcinoma of the prostate

local invasion and early metastasis in treatment-naive prostate cancer patients. We reconstructed evolutionary trajectories in five individuals, generating clone maps to visualise the spread and expansion of tumour clones. This approach revealed evolution primarily driven by SNVs in patient #02, from an ancestral clone with several copy number alterations. On the other hand, several copy number changes involving known cancer drivers were observed in patient #08, with extensive branching evolution within the prostate. These cases throw new light on the source of the extensive intra-tumour heterogeneity seen within prostate cancers, building on work reported by Cooper et al. [8], who depicted intra-tumour genomic heterogeneity using phylogenetic analysis of multi-region samples. The inclusion of seminal vesicle and lymph node samples revealed the specific clones that resulted in local invasion and metastasis.

Presence of cancer in the seminal vesicles is staged as T3b and is associated with worse prognosis than organ-confined disease. The SV samples in this study were

polyclonal, suggesting invasive spread from the prostate as the most likely mechanism, corroborating the findings from Woodcock et al. [11]. However, multi-clonal seeding through metastatic spread cannot be ruled out. In patient #10, lymph node metastases arose from the base of the prostate and the seminal vesicles, which concurs with the reports that seminal vesicle invasion is associated with metastasis and worse prognosis [39].

In patient #10, we show the genomic correlates involved in the transformation of adenocarcinoma to amphicrine morphology. Amphicrine cancer is a relatively rare subtype of prostate cancer having a distinctive morphology with synchronous dual exocrine and neuroendocrine (NE) differentiation. Morphologically, these tumours show solid/nested growth with cells with amphiphilic cytoplasm, vesicular nuclei and macronuclei, without the features of small cell or large cell NE carcinoma. Immunohistochemically, the tumours are positive for PSA, AR, ChromograninA or Synaptophysin and have a high Ki67 index (median 50%) [37]. While data are limited due to

its rarity, it is thought that amphicrine prostate cancer is often associated with metastatic disease [40] and may be responsive to AR-targeted therapy [41]. More recent work by Graham et al. suggests that there may be differences in the clinical outcomes of treatment-naïve and post-treatment amphicrine prostate cancer [42]. The nodal metastatic tumour in this case and some of the primary tumour showed extensive neuroendocrine (NE) differentiation. There was solid/nested growth with some gland formation in the primary tumour. Cells showed amphophilic cytoplasm, vesicular nuclei and macronucleoli, without the features of small cell or large cell NE carcinoma. The majority of the nodal metastatic disease showed solid sheets of high grade carcinoma cells with rosettes and small areas of necrosis. Immunohistochemistry performed as part of the diagnostic work up on the nodal tumour showed positive staining for androgen receptor (AR), NKX3.1, PSA polyclonal, and Synaptophysin. ChromograninA was negative. The proliferation index on Ki67 staining was 60%. The morphological features were not typical of small cell NE carcinoma and were considered those of the relatively recently described entity of 'Prostate Carcinoma with Amphicrine Features'. We were able to map the 3-dimensional spread of cancer in patient #10 using histopathology as a guide for sample selection. The spatially proximal but morphologically and genetically distinct areas within the same tumour have very different outcomes: the adenocarcinoma did not metastasise, whereas the adjacent amphicrine cancer metastasised to several lymph nodes. The amplification of 8q and loss of heterozygosity of 8p are prominent changes associated with the amphicrine transformation in this patient. The enhanced understanding of cancer spread in 3D in this patient also shows the limitation of representing clonal spread as 2D clone maps, as this is likely to be a simplification of a more complex series of events in the other patients.

In patient #15, we identified a whole genome duplication event; subclonality (copy number, SNVs) and genomic instability were also observed in the LPZLat sample. López et al. proposed that whole genome doubling could be a mechanism for reduced genomic instability [43]. PHH3 staining is specific for the M phase of the cell cycle [44], and hence, a higher staining in the LPZMid sample suggests a delayed cell cycle. Increased genomic complexity is thought to induce greater replication stresses [45] and upregulation of the NHEJ repair pathway in polyploid cells [46]. The increased but error-prone repair through the NHEJ pathway may explain the SBS3 signature in conjunction with WGD in patient #15. Taking these findings together with the increased immune cell infiltration in the pre-WGD region, we propose a model of tumour progression in patient #15

whereby increased genomic instability due to inactivation of TP53 could have resulted in rapid genomic changes, with such a region acting as a 'clone factory' where several daughter clones were produced. The high rate of mutations also could have led to increased immune surveillance, which combined with the effect of deleterious mutations caused most daughter clones to fail to survive. WGD acted as an escape mechanism by allowing repair of DNA damage through the NHEJ pathway. Thus, even though WGD cells may have a lower rate of growth due to cell cycle delay, they were better able to survive due to better tolerance to deleterious mutations and reduced immune surveillance.

Histopathological evaluation of tissue samples is central to prostate cancer diagnosis. Several morphological types have been described in prostate cancer, but we lack a clear understanding of the molecular mechanisms underlying these entities. It is likely that such causal mechanisms act at the DNA, RNA or protein levels. In this study, we identified several genomic changes (SNVs and CNAs) associated with a change in histological appearance. In all four instances of within-patient histological differences that we identified in this study, hundreds of unique SNVs place the distinct morphologies on separate branches of the evolutionary trees. Hence, histological heterogeneity in prostate cancer could represent later stages of divergent evolution. As branching evolution results in intra-tumour heterogeneity, and different branches allow distinct paths to disease progression (cancer drivers), the ability to identify the genomic 'branching-ness' of a prostate cancer sample by quantifying the morphological heterogeneity (e.g. by image analysis of biopsies) could function as a valuable screen to identify aggressive prostate cancers. However, this preliminary finding of a morpho-molecular link in a small set of patients must be validated further in a large patient cohort for potential prognostic utility. Our results also corroborate the previously reported finding that divergent lineages spatially coexist within the prostate [11]. Early work by Haffner et al. demonstrated the wealth of insights that can be drawn from multi-sample analysis in a single patient, identifying a histologically low grade prostate region as the source of the lethal metastatic clone [47]. Morphological features have been linked to molecular subtypes in other cancers [12, 48] and paradigms exist to combine both to predict patient outcomes [49]. In prostate cancer, specific morphological subtypes such as the cribriform pattern and intraductal carcinoma of the prostate have been linked with adverse outcomes [50, 51]. Hence, our findings provide a strong case for histopathologically guided genomic studies to identify specific mutations associated with distinct morphologies at the cellular or glandular level, as well as to

develop diagnostic methods that combine histological and genomic data.

Conversely, not all mutations are associated with a change in morphology; the Anterior sample from patient #10 annotated as ‘benign’ histologically was found to harbour a cluster of ~250 SNVs representing a mutant clone, independent from the main cancer lineage. Cooper et al. [8] and Erickson et al. [52] demonstrated previously the presence of SNVs and copy number changes in histologically normal regions. Such regions may represent foci of early clonal expansion from a lineage distinct from the main tumour. In addition, Boutros et al. [53] and Espiritu et al. [54] found tumour clones of independent prostate cancer lineages, indicating that this is not uncommon in prostate cancer.

## Conclusions

Taken together, we successfully integrated whole-genome sequencing with histopathological data to unravel the source of intra-tumour histological and clonal heterogeneity in locally advanced prostate cancer. Using this approach, we obtained several new biological insights including identification of the genomic mechanism for the origin of amphicrine carcinoma of the prostate, and construction of detailed maps of intra-prostatic tumour evolution. We showed that morphologically distinct regions of cancer represent separate branches of evolution, which has implications for diagnosis. These insights will pave the way to develop novel tools to identify features of the prostate cancer metastatic and lethal phenotype, which in turn will allow early interventions where necessary and improved patient outcomes.

## Supplementary Information

The online version contains supplementary material available at <https://doi.org/10.1186/s13073-024-01302-x>.

**Additional file 1.** Supplementary figures supporting findings described in the main text.

**Additional file 2.** Cancer Cell Fraction (CCF) tables for each patient.

**Additional file 3.** List of samples analysed in the study, with patient numbers and anatomical locations (comma separated value file – plain text).

## Acknowledgements

We acknowledge the contribution to this study made by the Oxford Centre for Histopathology Research and the Oxford Radcliffe Biobank. We thank the Wellcome Trust Centre for Human Genetics, Oxford, and Wales Gene Park, Cardiff, for sequencing services. Wales Gene Park is an infrastructure support group with funding from Welsh Government through Health and Care Research Wales. The computational aspects of this research were funded from the NIHR Oxford BRC with additional support from the Wellcome Trust Core Award Grant Number 203141/Z/16/Z. The views expressed are those of the author(s) and not necessarily those of the NHS, the NIHR or the Department of Health.

## Authors' contributions

SR, LC, ZK and MJ performed laboratory experiments. SR, CV, DJW, NKA, FB and DCW generated and analysed data. SR, CV and DJW interpreted the results.

CV, MO'H, AH and AL, curated and biobanked patient samples. ADL, ITul, JN, SL, AO, FL and TL were involved in surgical sample collection. FH, IT and BV procured funding and supervised the project. SR wrote the manuscript with input from CV, DJW, FH, IT, IM, ADL and RB. SR and CV contributed equally. All authors read and approved the final manuscript.

## Funding

We are grateful to Cancer Research UK (C1380/A18444) and NIHR Oxford BRC Surgical Innovation Theme for funding this research. DCW is part funded by Cancer Research UK RadNet Manchester (C1994/A28701) and is supported by the NIHR Manchester Biomedical Research Centre (NIHR203308).

## Availability of data and materials

Sequencing data are available at the European Genome-Phenome archive (EGAD00001011174) [55] and code used for SNV clustering is available on GitHub [56].

## Declarations

### Ethics approval and consent to participate

Patients consented to participate in this study under Research Ethics Committee approval no. 18/SC/0103, and formalin-fixed, paraffin-embedded samples were obtained through the routine histopathological diagnostic pathway under Oxford Radcliffe Biobank ethics (Research Ethics Committee approval no. 19/SC/0173) from patients who consented as above. This research conformed to the principles of the Helsinki Declaration.

### Consent for publication

Not applicable.

### Competing interests

ADL has received educational support and funding to attend meetings from Intuitive Surgical and BXT Accelyon. While acting as Chief investigator of ProMOTe Trial (2022–2023), he benefited from payment-in-kind support from Imaginab & Catalent for IAB2M-IR800 stability testing. He was a signatory/author of the ‘TREXIT’ paper for prostate biopsy. He is co-PI of the TRANSLATE trial funded by NIHR(HTA) and lead investigator of the QUANTUM Biobank part funded by the John Black Charitable Foundation. He is personally funded by Cancer Research UK (C57899/A25812) who also fund his SPACE Study lab. He has previously received grant funding from Prostate Cancer UK (PA14-022), The Academy of Medical Sciences (SGCL11), Medical Research Council (CIC), Cambridge BRC and GlaxoSmithKline. He has received education support from Astellas, Lilly, AstraZeneca and Ipsen. He is a stipendiary BJUI Section Editor for Prostate Cancer and has received honoraria for reviewing for European Urology and Lancet Oncology. He has received consulting fees from AlphaSights. The other authors declare that they have no competing interests.

### Author details

<sup>1</sup>Nuffield Department of Surgical Sciences, University of Oxford, Oxford, UK. <sup>2</sup>Nuffield Department of Orthopaedics, Rheumatology and Musculoskeletal Sciences, University of Oxford, Oxford, UK. <sup>3</sup>Department of Oncology, University of Oxford, Oxford, UK. <sup>4</sup>Manchester Cancer Research Centre, University of Manchester, Manchester, UK. <sup>5</sup>Botnar Research Centre, Windmill Road, Oxford OX3 7LD, UK.

Received: 19 July 2023 Accepted: 6 February 2024

Published online: 19 February 2024

## References

- Gordetsky J, Epstein J. Grading of prostatic adenocarcinoma: current state and prognostic implications. *Diagn Pathol.* 2016;11:25.
- Montironi R, Cimadamore A, Cheng L, Lopez-Beltran A, Scarpelli M. Prostate cancer grading in 2018: limitations, implementations, cribriform morphology, and biological markers. *Int J Biol Markers.* 2018;33:331–4.
- van Leenders GJLH, Verhoef EI, Hollemans E. Prostate cancer growth patterns beyond the Gleason score: entering a new era of comprehensive tumour grading. *Histopathology.* 2020;77:850–61.

4. Wright JL, et al. Prostate cancer specific mortality and Gleason 7 disease differences in prostate cancer outcomes between cases with Gleason 4 + 3 and Gleason 3 + 4 tumors in a population based cohort. *J Urol.* 2009;182:2702–7.
5. Bryant RJ, et al. The ProtecT trial: analysis of the patient cohort, baseline risk stratification and disease progression. *BJU Int.* 2020;125:506–14.
6. Haffner MC, et al. Genomic and phenotypic heterogeneity in prostate cancer. *Nat Rev Urol.* 2021;18:79–92.
7. Brady L, et al. Inter- and intra-tumor heterogeneity of metastatic prostate cancer determined by digital spatial gene expression profiling. *Nat Commun.* 2021;12:1426.
8. Cooper CS, et al. Analysis of the genetic phylogeny of multifocal prostate cancer identifies multiple independent clonal expansions in neoplastic and morphologically normal prostate tissue. *Nat Genet.* 2015;47:367–72.
9. Wedge DC, et al. Sequencing of prostate cancers identifies new cancer genes, routes of progression and drug targets. *Nat Genet.* 2018;50:682–92.
10. Gundem G, et al. The evolutionary history of lethal metastatic prostate cancer. *Nature.* 2015;520:353–7.
11. Woodcock DJ, et al. Prostate cancer evolution from multilineage primary to single lineage metastases with implications for liquid biopsy. *Nat Commun.* 2020;11:5070.
12. Lomakin A, et al. Spatial genomics maps the structure, character and evolution of cancer clones. 2021. 2021.04.16.439912 Preprint at <https://doi.org/10.1101/2021.04.16.439912>.
13. Zhao T, et al. Spatial genomics enables multi-modal study of clonal heterogeneity in tissues. *Nature.* 2022;601:85–91.
14. Nurminen A, et al. Cancer origin tracing and timing in two high-risk prostate cancers using multisample whole genome analysis: prospects for personalized medicine. *Genome Med.* 2023;15:82.
15. Fu Y, et al. Pan-cancer computational histopathology reveals mutations, tumor composition and prognosis. *Nat Cancer.* 2020;1–11. <https://doi.org/10.1038/s43018-020-0085-8>.
16. Kather JN, et al. Pan-cancer image-based detection of clinically actionable genetic alterations. *Nat Cancer.* 2020;1:789–99.
17. Gill PS, et al. The handling and sampling of radical prostatectomy specimens for reporting and research: the Oxford approach. *J Clin Pathol.* 2012;65:1057–61.
18. Ellis P, et al. Reliable detection of somatic mutations in solid tissues by laser-capture microdissection and low-input DNA sequencing. *Nat Protoc.* 2021;16:841–71.
19. BBMap. SourceForge <https://sourceforge.net/projects/bbmap/>.
20. Andrews S. FastQC: a quality control tool for high throughput sequence data. 2010. <https://www.bioinformatics.babraham.ac.uk/projects/fastqc/>.
21. Li H. Aligning sequence reads, clone sequences and assembly contigs with BWA-MEM. 2013. Preprint at <https://doi.org/10.48550/arXiv.1303.3997>.
22. Danecek P, et al. Twelve years of SAMtools and BCFtools. *GigaScience.* 2021;10:giab008.
23. Van der Auwera GA, et al. From FastQ data to high-confidence variant calls: the genome analysis toolkit best practices pipeline. *Curr Protoc Bioinforma.* 2013;43:11.10.1-11.10.33.
24. Nik-Zainal S, et al. The life history of 21 breast cancers. *Cell.* 2012;149:994–1007.
25. DPCLust pre-processing. Wedge lab. 2022.
26. Pedregosa F, et al. Scikit-learn: machine learning in Python. *J Mach Learn Res.* 2011;12:2825–30.
27. Tarabichi M, et al. A practical guide to cancer subclonal reconstruction from DNA sequencing. *Nat Methods.* 2021;18:144–55.
28. Plotly Technologies Inc. Collaborative data science. Plotly Technologies Inc; 2015.
29. Rosenthal R, McGranahan N, Herrero J, Taylor BS, Swanton C. Deconstruct-Sigs: delineating mutational processes in single tumors distinguishes DNA repair deficiencies and patterns of carcinoma evolution. *Genome Biol.* 2016;17:31.
30. Wala JA, et al. SvABA: genome-wide detection of structural variants and indels by local assembly. *Genome Res.* 2018;28:581–91.
31. Hafstað V, Häkkinen J, Persson H. Fast and sensitive validation of fusion transcripts in whole-genome sequencing data. *BMC Bioinformatics.* 2023;24:359.
32. R Core Team. R: a language and environment for statistical computing. Vienna, Austria: R Foundation for Statistical Computing; 2022.
33. Van Rossum G, Drake FL. Python 3 Reference Manual. Scotts Valley, CA: CreateSpace; 2009.
34. Martínez-Jiménez F, et al. A compendium of mutational cancer driver genes. *Nat Rev Cancer.* 2020;1–18. <https://doi.org/10.1038/s41568-020-0290-x>.
35. Robinson M, et al. Quality assurance guidance for scoring and reporting for pathologists and laboratories undertaking clinical trial work. *J Pathol Clin Res.* 2019;5:91–9.
36. Takayama K, et al. Integrative analysis of FOXP1 function reveals a tumor-suppressive effect in prostate cancer. *Mol Endocrinol.* 2014;28:2012–24.
37. Prendeville S, et al. Prostate carcinoma with amphicrine features: further refining the spectrum of neuroendocrine differentiation in tumours of primary prostatic origin? *Histopathology.* 2017;71:926–33.
38. Fine SW. Neuroendocrine tumors of the prostate. *Mod Pathol.* 2018;31:122–32.
39. Mottet N, et al. EAU-EANM-ESTRO-ESUR-SIOG guidelines on prostate cancer—2020 update. Part 1: screening, diagnosis, and local treatment with curative intent. *Eur Urol.* 2021;79:243–62.
40. Bellur S, Van der Kwast T, Mete O. Evolving concepts in prostatic neuroendocrine manifestations: from focal divergent differentiation to amphicrine carcinoma. *Hum Pathol.* 2019;85:313–27.
41. Labrecque MP, Alumkal JJ, Coleman IM, Nelson PS, Morrissey C. The heterogeneity of prostate cancers lacking AR activity will require diverse treatment approaches. *Endocr Relat Cancer.* 2021;28:T51–66.
42. Graham LS, et al. Clinical, pathologic, and molecular features of amphicrine prostate cancer. *Prostate.* 2023. <https://doi.org/10.1002/pros.24497>.
43. López S, et al. Interplay between whole-genome doubling and the accumulation of deleterious alterations in cancer evolution. *Nat Genet.* 2020;52:283–93.
44. Ren J, et al. Identification of G2/M phase transition by sequential nuclear and cytoplasmic changes and molecular markers in mice intestinal epithelial cells. *Cell Cycle.* 2018;17:780–91.
45. Wangsa D, et al. Near-tetraploid cancer cells show chromosome instability triggered by replication stress and exhibit enhanced invasiveness. *FASEB J.* 2018;32:3502–17.
46. Zheng L, et al. Polyploid cells rewire DNA damage response networks to overcome replication stress-induced barriers for tumour progression. *Nat Commun.* 2012;3:815.
47. Haffner MC, et al. Tracking the clonal origin of lethal prostate cancer. *J Clin Invest.* 2013;123:4918–22.
48. Sirinukunwattana K, et al. Image-based consensus molecular subtype (imCMS) classification of colorectal cancer using deep learning. *Gut.* 2021;70:544–54.
49. Mobadersany P, et al. Predicting cancer outcomes from histology and genomics using convolutional networks. *Proc Natl Acad Sci.* 2018;115:E2970–9.
50. Böttcher R, et al. Cribriform and intraductal prostate cancer are associated with increased genomic instability and distinct genomic alterations. *BMC Cancer.* 2018;18:8.
51. Chua MLK, et al. A prostate cancer “nimbus”: genomic instability and SchLAP1 dysregulation underpin aggression of intraductal and cribriform subpathologies. *Eur Urol.* 2017;72:665–74.
52. Erickson A, et al. Spatially resolved clonal copy number alterations in benign and malignant tissue. *Nature.* 2022;608:360–7.
53. Boutros PC, et al. Spatial genomic heterogeneity within localized, multifocal prostate cancer. *Nat Genet.* 2015;47:736–45.
54. Espiritu SMG, et al. The evolutionary landscape of localized prostate cancers drives clinical aggression. *Cell.* 2018;173:1003–1013.e15.
55. Rao SR. Intra-prostatic tumour evolution, steps in metastatic spread and histogenomic associations revealed by integration of multi-region whole genome sequencing with histopathological features - Whole Genome Sequencing data. EGA European Genome-Phenome Archive; 2023. <https://ega-archive.org/datasets/EGAD00001011174>.
56. Rao SR. Python code used for SNV clustering. GitHub; 2023. [https://github.com/sraoro/promote\\_genomics\\_manuscript](https://github.com/sraoro/promote_genomics_manuscript).

## Publisher's Note

Springer Nature remains neutral with regard to jurisdictional claims in published maps and institutional affiliations.